

1 **Machine Learning Predicts the Timing and Shear Stress Evolution of Lab Earthquakes**
2 **Using Active Seismic Monitoring of Fault Zone Processes**

3
4 **Srisharan Shreedharan^{1*}, David Chas Bolton¹, Jacques Rivière², Chris Marone^{1,3}**

5
6 ¹Dept. of Geosciences, Pennsylvania State University, University Park, PA 16802 USA

7 ²Dept. of Engineering Science and Mechanics, Pennsylvania State University, University Park,
8 PA 16802 USA

9 ³Dipartimento di Scienze della Terra, La Sapienza Università di Roma, Italy

10
11
12 ***Corresponding author: srisharan@psu.edu**

17 **Abstract:**

18 Machine learning (ML) techniques have become increasingly important in seismology and
19 earthquake science. Lab-based studies have used acoustic emission data to predict time-to-
20 failure and stress state, and in a few cases the same approach has been used for field data.
21 However, the underlying physical mechanisms that allow lab earthquake prediction and seismic
22 forecasting remain poorly resolved. Here, we address this knowledge gap by coupling active-
23 source seismic data, which probe asperity-scale processes, with ML methods. We show that
24 elastic waves passing through the lab fault zone contain information that can predict the full
25 spectrum of labquakes from slow slip instabilities to highly aperiodic events. The ML methods
26 utilize systematic changes in p-wave amplitude and velocity to accurately predict the timing and
27 shear stress during labquakes. The ML predictions improve in accuracy closer to fault failure,
28 demonstrating that the predictive power of the ultrasonic signals improves as the fault
29 approaches failure. Our results demonstrate that the relationship between the ultrasonic
30 parameters and fault slip rate, and in turn, the systematically evolving real area of contact and
31 asperity stiffness allow the gradient boosting algorithm to ‘learn’ about the state of the fault and
32 its proximity to failure. Broadly, our results demonstrate the utility of physics-informed machine
33 learning in forecasting the imminence of fault slip at the laboratory scale, which may have
34 important implications for earthquake mechanics in nature.

35

36 **Keywords:**

37 Stick-slips; slow earthquakes; Friction; Machine Learning; Gradient boosted trees; XGBoost

38 **Key points:**

- 39 1. Machine learning can be used on p-wave amplitude and velocity to predict the timing and
40 shear stress evolution of laboratory seismicity.
- 41 2. The ability of the ML algorithm to predict time-to-failure improves as the fault approaches
42 failure.
- 43 3. Predictions rely on the systematic reduction in elastic properties prior to failure, which is
44 linked to a reduction in real area of contact.

45 1. Introduction:

46 Machine learning (ML) methods have followed improvements in geophysical techniques,
47 instrumentation and data availability over the past decade to rapidly emerge as indispensable
48 toolkits for the geophysical community (*Bergen et al., 2019; Kong et al., 2019*). For instance,
49 significant effort has been devoted to using ML to improve event detection, arrival-time picking,
50 phase association, and earthquake location (*Yoon et al., 2015; Zhu and Beroza, 2018; Ross et al.,*
51 *2018; Perol et al., 2018; Wu et al., 2018; McBrearty et al, 2019; Trugman and Ross, 2019;*
52 *Mousavi et al., 2020*). Importantly, this has seen a revival in earthquake forecasting research,
53 particularly focused on applying ML techniques to lab data on fault friction (*Rouet-Leduc et al.,*
54 *2017, 2018*) and rock damage (*McBeck et al., 2020*) to infer failure modes and predictability
55 (*Corbi et al., 2019*). Notably, recent studies have successfully demonstrated that both cataloged
56 (*Lubbers et al., 2018*) and continuous (*Rouet-Leduc et al., 2017; Hulbert et al., 2019*) acoustic
57 emission (AE) data can be used to infer fault friction and predict the timing, shear stress, and in
58 some cases the size of labquakes. Moreover, ML has been used to demonstrate that slow and fast
59 earthquakes share similar physics (*Hulbert et al., 2019*). With varying degrees of success, these
60 techniques can predict field observations of volcanic eruption (*Ren et al., 2020*) and subduction
61 zone fault slip (*Rouet-Leduc et al., 2019; Corbi et al., 2020; Hulbert et al., 2020*).

62 Broadly, ML techniques can be grouped as supervised or unsupervised. The former
63 involves predetermined features that are mapped to labeled datasets in order to construct a
64 regression model that typically involves highly non-linear functions. Unsupervised learning
65 models are used where such labeled datasets may not be available or the focus is on trying to
66 identify patterns embedded within the data (e.g., *Tan et al., 2006; Oliver et al., 2018; Bolton et*
67 *al., 2019*). Especially as applied to laboratory data, supervised ML techniques have relied on

68 systematic evolution of ‘features’ such as the AE energy (e.g., *Rouet-Leduc et al., 2017, 2018*).
69 Indeed, based on the existing works, one could conclude that systematic changes in
70 microseismicity (AE) indicative of fault zone criticality are required to successfully predict
71 labquakes or tectonic fault slip. However, while precursors are routinely documented in
72 laboratory studies of fault failure and brittle fracturing (*Brace et al., 1966; Scholz, 1968a;*
73 *Sammonds et al., 1992; Hedayat et al., 2014; Kaproth and Marone, 2013; Scuderi et al., 2016;*
74 *Shreedharan et al., 2020*), observations of systematic precursors or foreshocks prior to
75 earthquakes in nature are not routinely documented (*Bakun et al., 2005; Niu et al., 2008; Main et*
76 *al., 2012*). Additionally, even when precursory slip is present, it may be masked by changes in
77 elastic properties of the wallrock (*Chiarabba et al., 2020; Shreedharan et al., 2021*). Moreover,
78 the underlying physics of ML prediction of lab earthquakes is poorly understood. One recent
79 study by *Bolton et al. (2020)* demonstrated that the precursory increase in AE energy prior to
80 fault failure is likely linked to preseismic fault slip. Thus, the question arises of whether
81 detection of preseismic fault slip and lab foreshocks are necessary conditions for ML-based
82 prediction of lab earthquakes, and ultimately, whether the same is true for field observations.

83 Here, we use high-resolution time-lapse active seismic monitoring to document the
84 evolution of p-wave amplitude and velocity during the lab seismic cycle of highly variable and
85 aperiodic labquakes. We find that the gradient boosting ML algorithm (*Friedman, 2001*) can
86 accurately predict both the timing and shear stress state of labquakes using a subset of the
87 amplitude and velocity features. Interestingly, our results show that the ML predictive power
88 improves as the fault approaches failure. Our previous works and those of others have
89 established the physical links between systematic variations in ultrasonic attributes (p-wave
90 amplitudes and velocities), fault zone preslip and wallrock stiffening throughout the laboratory

91 seismic cycle (*Shreedharan et al., 2020, 2021*). Further, these ultrasonic attributes can be linked
92 to asperity scale mechanical parameters such as the real area of contact and asperity stiffness
93 (*Kendall and Tabor, 1971; Pyrak-Nolte et al., 1990; Hedayat et al., 2014; Kilgore et al., 2017;*
94 *Shreedharan et al., 2019*). Thus, by successfully training our ML algorithm on these ultrasonic
95 attributes, we assign a physical underpinning for the predictive power of the ML approach.

96

97 **2. Methods:**

98 *2.1. Friction experiments*

99 We performed frictional shear experiments in a servo-controlled biaxial testing apparatus
100 using a double-direct shear (DDS) configuration (*Karner and Marone, 1998*). We sheared two
101 frictional interfaces created by mating three blocks of Westerly granite, with a fine layer (<200
102 μm thickness and ~ 0.25 g/layer by mass) of quartz powder between the interfaces to simulate
103 frictional wear material (Figure 1; Also see *Shreedharan et al., 2020*). The granite surfaces were
104 roughened with #60 grit silicon carbide thus producing a mean roughness of ~ 20 μm . The
105 surface roughness and the dusting of quartz powder (median particle size of 10.5 μm) have
106 comparable dimensions; thus frictional processes include direct contact of the wall rock, wear,
107 and internal deformation in the gouge. The fault normal stress was held constant via a fast-acting
108 servocontroller. The biaxial testing apparatus is fully servo-controlled with independent
109 hydraulic pistons supplying normal and shear loads. The experiments were instrumented with
110 calibrated strain-gauge load cells to measure normal and shear stresses, and direct current
111 differential transformers (DCDTs) to measure fault normal and shear displacement. An
112 additional DCDT was attached to the center block close to one of the frictional interfaces, to
113 measure fault slip (Figure 1). All load cells used in this study have a resolution of ± 5 N and the

114 DCDTs have a displacement resolution of $\pm 0.1 \mu\text{m}$. We acquired mechanical data at 10 kHz and
 115 averaged in real-time to 100 or 1000 Hz prior to recording. A constant shear displacement rate
 116 was prescribed for the longer, central block of the DDS configuration. In all experiments
 117 reported here, the samples had a constant nominal frictional contact area of 25 cm^2 and were
 118 subjected to a 10 MPa normal stress. The prescribed background shear rate was set at $11 \mu\text{m/s}$.
 119 All experiments were performed at a nominal room temperature range of $22 - 24 \text{ }^\circ\text{C}$ and the
 120 sample humidity was maintained at 100% to ensure reproducibility. We produced a spectrum of
 121 slip modes from slow to fast (Inset to Figure 1; *Leeman et al., 2016*) by varying the stiffness of
 122 the shear loading system (*Shreedharan et al., 2020*).

123

124 2.2. Ultrasonic monitoring

125 We conducted continuous seismic monitoring via ultrasonic pulses transmitted through
 126 the fault interfaces. We used 500 kHz broadband, P-polarized lead-zirconate-titanate (PZT)
 127 crystals (Boston Piezo-Optics Inc. PZT-5A 0.5" diameter) and transmitted half-sine pulses every
 128 1 ms continuously throughout frictional shear. The PZT sensors were epoxied in blind holes
 129 within steel platens and positioned adjacent to the granite side blocks of the DDS configuration
 130 (See inset to Figure 1). Each pulse was sampled at 25 MHz, thus ensuring high temporal
 131 resolution in sampling. We use the first P-wave arrival to calculate travel-times and velocities,
 132 and take the largest peak-to-peak amplitude within the first $5 \mu\text{s}$ for acoustic transmissivity (Inset
 133 to Figure 1). Following *Nagata et al. (2014)*, we report transmissivity, $|T|$, as

$$134 \quad |T| = \sqrt{\frac{A_{DDS}}{A_{Intact}}} \quad (1)$$

135 In Eq. (1), the square root term accounts for the two frictional interfaces that the
 136 ultrasonic pulses traverse (*Shreedharan et al., 2019*). We calculate the velocity as the ratio of the

137 distance traversed by the wavelet to the travel time through the DDS blocks, after accounting for
138 the time spent in steel and at interfaces. We refer readers to *Shreedharan et al. (2021)* for a
139 detailed description of our velocity and transmissivity measurements.

140

141 *2.3. ML model – training and testing*

142 We analyze the acoustic and mechanical data using ML to predict the temporal evolution
143 of shear stress and the time remaining prior to failure for multiple laboratory seismic cycles
144 (Figure 2). Because we use a supervised learning approach, our first step involves data
145 preparation and selection of features and labelled datasets. Previous studies have demonstrated
146 that the P-wave amplitudes and velocities evolve systematically throughout the lab seismic cycle.
147 This, in addition to their direct proxy relationship to asperity deformation mechanics, makes
148 them good candidate features for our model. The labelled data, i.e., the ‘unknown’ datasets that
149 we want to predict are the fault shear stress, time since the previous failure event and,
150 importantly, the time remaining until failure. Figures 2a-b show the labelled data and Figures 2c-
151 d show the features used in this study. Note that while the shear stress is readily determined as
152 part of regular data collection during the experiment, the time-since-failure and time-to-failure
153 labels are measured from the shear stress data. The time-since-failure for an event is computed
154 from the shear stress minimum of the previous event, which has a time-since-failure label of 0 s,
155 to the shear stress maximum for the next event. Conversely, the time-to-failure for each stick-
156 slip cycle is counted from the shear stress minimum at the end of the previous cycle, up to the
157 shear stress maximum corresponding to the current cycle, which represents a time to failure of 0
158 s (Figure 2b). During the coseismic portion of the cycle, i.e., the stress drop, the time-since and
159 time-to-failure are set to zero and these data are not used for the ML regression.

160 As part of feature preparation, we smooth the features using a backward-looking 10-point
161 moving average to reduce feature-side noise in the ML regression. We then normalize the
162 features for each labquake against the minimum value of the feature at the end of the previous
163 cycle (Figure 2e-f). This is done to ensure that long-term trends in the features due to layer-
164 thinning, shear localization, wear product formation and smoothening of the granite surfaces do
165 not overprint on their shorter-term evolution during the slip instabilities. Further, this ensures
166 that the features in any slip instability are independent and have no ‘memory’ of the fault’s
167 previous state in an earlier cycle. As a final feature engineering step, we estimate a time-
168 advanced version of the feature (amplitude or velocity). This is done by shifting the feature
169 vector forward by five time steps (0.05 s). We use the original feature corresponding to time t
170 and a time-advanced feature corresponding to time $t - 0.05$ s in our regression. The temporal
171 evolution of the amplitude and velocity features includes an increasing and comparably
172 decreasing gradient. When regressing these features against a monotonically varying label such
173 as shear stress or time to failure, there ceases to exist a one-to-one functional mapping, i.e., non-
174 unique solutions. This results in poor performance by regression-based supervised learning
175 techniques, as noted by previous works (*Rouet-Leduc et al.*, 2017) because, for a given stick-slip,
176 two data labels can correspond to the same feature value. We conducted a series of
177 benchmarking tests and found that this ‘offsetting’ procedure solves the problem by informing
178 the ML models whether the feature corresponding to a data label comes from the increasing or
179 decreasing gradient space. Additionally, because we use a time-advanced offset, the new offset
180 feature is backward-looking in time, thus eliminating any potential data leakage issues. This
181 method is similar to and was derived from the sub-windowing procedure utilized by *Hulbert et*
182 *al.* (2019) to solve a similar functional mapping problem in their ML regression. We note here

183 that the offsetting is a mathematical transformation rather than a physical one. Hence, the choice
184 of an n -point offset is arbitrary and this parameter, in general, can and should be optimized to
185 ensure good fits to the labelled data. We selected a 5-point offset for this study since it provided
186 excellent fits to the test data without overfitting the training data.

187 Subsequently, we split our labeled dataset and features into training and testing sets
188 (Figure 1). In this study, we report on the results from a 70-30 split in a contiguous fashion, i.e.,
189 the initial 70% of the data were designated as the training set and the remaining 30% as the test
190 dataset. Note that, unlike previous ML studies on experimental faults, which make use of
191 windowing procedures to estimate features (*Rouet-Leduc et al., 2017; Hulbert et al., 2019;*
192 *Bolton et al., 2019; Corbi et al, 2019*), our mechanical and ultrasonic data are synchronized in
193 time. In other words, for each temporally evolving value of the labels (shear stress, time-since-
194 failure, time-to-failure), there exists a corresponding data-point in the feature-space (amplitudes,
195 velocities).

196 We use the gradient boosting ML algorithm based on decision trees (*Friedman, 2001;*
197 *Hulbert et al., 2019*), to jointly analyze our acoustic and mechanical datasets. Specifically, we
198 utilize an open-source implementation of this algorithm named XGBoost (*Chen and Guestrin,*
199 *2016*). Hyperparameter tuning is the first step in implementing this model. Hyperparameters
200 define and determine the parameter-space of functions that can serve as potential models, and the
201 model performance is significantly sensitive to the assigned hyperparameters. The XGBoost
202 implementation has a suite of hyperparameters which must be optimized prior to training. In this
203 study, we determine the optimal hyperparameters by implementing an Efficient Global
204 Optimization (EGO) function to minimize a misfit function (*Jones et al., 1998*). The optimal
205 hyperparameters are determined via a five-fold cross-validation. Here, a subset of the training

206 data is modeled using a given set of hyperparameters and validated against the remaining
207 training data. Once the hyperparameter ‘tuning’ step is complete, we train the ML model by
208 performing regressions on the feature-label relationship. This step involves iteratively
209 developing the structure of the gradient boosted decision trees. For a detailed description of this
210 method, we refer the readers to the XGBoost documentation (xgboost.readthedocs.io) and
211 *Hulbert et al. (2019)*. Finally, the optimal model is tested and its performance is compared
212 against the labels, i.e., the true experimental values of shear stress and time to failure. We
213 evaluate the model performance in two ways: (1) a qualitative benchmark against a naïve
214 constant-recurrence interval model for the time-to-failure and (2) a quantitative estimation of the
215 model performance using the coefficient of determination (R^2) and the root mean squared error
216 (RMSE) for all labelled data.

217

218 **3. Results:**

219 *3.1. Friction data and stick-slip periodicity*

220 Our lab results include the full spectrum of frictional slip modes from slow to fast
221 labquakes. In particular, the experimental data are characterized by a range of aperiodic frictional
222 slip instabilities (Figure 3) at the friction stability boundary (e.g., *Gu et al., 1984; Leeman et al.,*
223 *2016*). Figure 3a quantifies this frictional chaos by plotting the inter-event times as a cross-plot
224 of time since the last instability T_{prev} and time to the next instability T_{next} (See inset to Figure 1).
225 Data that fall on the 1:1 line represent perfect periodicity, i.e., they are time and slip predictable
226 events (eg. *Shimazaki and Nakata, 1980*). The 1:2 and 2:1 lines form an envelope representing
227 period doubling (*Veedu et al., 2020*). Further, data points are colored by the magnitude of stress
228 drop for these events. Broadly, while our data have periodicities between perfectly periodic and

229 doublets, the higher stress drop events are generally represented by more aperiodic behavior
230 while the smaller events cluster tightly around the 1:1 line.

231 We observe that stick-slip instability behavior and frictional chaos evolves with shear
232 displacement, represented by increasing event number (Figure 3). Event numbers are calculated
233 from the ML train-test catalog (Figure 1), i.e., between load point displacements of 18 – 21 mm,
234 which contains 220 events. While the peak stress remains relatively constant throughout shear,
235 the stress minimum during the coseismic phase increases with shear (Figure 3b). In other words,
236 the fault starts off in a quasi-stable condition and becomes increasingly unstable. This is a
237 common observation related to shear driven reduction in the friction critical slip distance (D_c)
238 and increase in the friction rate parameter, $(b-a)$, within the rate-state frictional framework (e.g.,
239 *Marone, 1998b*). The inter-event ratio from Figure 3a is plotted in Figure 3c as a function of
240 event number, which is used here as a proxy for shear displacement. For the first ~50 events, the
241 slip behavior is relatively periodic. As the stress drop increases with shear, the slip behavior
242 becomes increasingly complex which makes this an ideal dataset to challenge ML approaches for
243 prediction.

244

245 *3.2. Co-evolution of friction and elastic properties*

246 Fault zone elastic properties and frictional strength co-evolve in a systematic manner
247 during the lab seismic cycle (Figure 4). The fault zone elastic wave amplitude and velocity co-
248 evolve with shear stress and fault slip rate during both slow and fast slip lab earthquakes (Figure
249 4a). The corresponding fault displacement, obtained from an onboard displacement sensor (Inset
250 to Figure 1) and slip velocity, measured from the time derivative of this fault slip, also increase
251 systematically as the fault approaches failure (Figure 4b). For our loading rate of 11 $\mu\text{m/s}$ the

252 fault experiences peak slip rates of $\sim 300 \mu\text{m/s}$, and interseismic locking rates of under $0.1 \mu\text{m/s}$
253 for the largest, fastest events. The corresponding transmissivity and p-wave velocities are shown
254 in Figures 4c-d. Note the strong inverse correlation between fault slip rate and the ultrasonic
255 attributes, which is consistent with observations from previous ultrasonic studies of laboratory
256 stick-slips (Nagata *et al.*, 2014; Kilgore *et al.*, 2017; Shreedharan *et al.*, 2020, 2021).

257

258 *3.3. Machine learning models of shear stress, time-since and time-to-failure*

259 We document the training, testing and performance metrics of the XGBoost models for
260 shear stress, time-since-failure and time-to-failure labels in Figures 5-7. For each label, we train
261 and test three ML models: one for transmitted wave amplitude, one for velocity, and one for the
262 combined features of amplitude and velocity. We do not use a separate validation set; rather we
263 perform a five-fold cross-validation on the training datasets.

264 We report the ML results of shear stress prediction using transmissivity (and its offset) as
265 the sole feature (Figure 5a-b) and velocity (and its offset) as the sole feature (Figure 5d-e). Here,
266 we quantify the model performance using a standard R^2 metric (Figure 5). Models trained with
267 both amplitude and velocity have higher R^2 metrics for training compared to the test set (Figure
268 5), which is nominally expected since the models are bound to perform better on datasets they
269 have previously ‘seen.’ Regardless, the test set has a reasonable model performance of $R^2 = 0.80$
270 for both amplitude and velocity-based ML models. Cross-plots of ML model estimates and
271 experimentally measured values of shear stress show the model performance (Figures 5c,f), with
272 the solid (1:1) line representing perfect predictions. We observe that the models tend to deviate
273 from the experimental data early in the seismic cycle, i.e., the shear stress minima, and close to
274 the middle of the cycle, approximately where the amplitudes and velocity features switch from

275 an increasing to decreasing gradient. However, the ML model performance improves as time to
276 failure decreases (Figure 5g/h). For both amplitude and velocity-based ML models the root
277 mean squared error (RMSE) calculated over a 10-point moving window shows somewhat poor
278 performance early in the lab seismic cycle (i.e., at ~ 3555.4 s) but improved performance later in
279 the cycle, i.e., between 3556 – 3557 s (Figure 5g/h).

280 Figure 6 shows a snapshot of the results from a training and testing exercise on the time-
281 since-failure data label. The ML performance using amplitudes and velocities as features are
282 shown in Figures 6a-c and 6d-f respectively. The ML models perform better during the early
283 parts of the seismic cycle (Figure 6c/f). In other words, the time-since-failure label is best
284 predicted by the early portions of the amplitude and velocity evolution, immediately following a
285 seismic event. Zooms of representative time-since-failure evolution over one seismic cycle, show
286 the corresponding ML model and 10-point windowed RMSE evolution (Figures 6g-h). These
287 plots show the superior fits to the experimental data early in the seismic cycle. Specifically, the
288 RMSE is lowest (or nearly 0) in the initial ~ 1 s following a stick-slip event and then continually
289 increases until the next stick-slip event.

290 ML models focused on the time-to-failure label are the most pertinent for earthquake
291 forecasting. Figures 7a-c show the results from a ML model created using amplitudes as the
292 primary feature, and Figures 7d-f show the results from a model using velocities. Generally, we
293 document poor performance early in the cycle (see Figures 7c,f between 2-4 s) when the time-to-
294 failure is highest. The model fits improve as the fault approaches failure. Figures 7g-h show
295 representative stick-slip cycles with their associated RMSE for the amplitude- and velocity-
296 trained ML models. Again, we document a reducing RMSE as the fault approaches failure, i.e.,

297 as the time-to-failure approaches zero, particularly in the final ~0.8 s or final ~22% of the
298 interseismic period.

299

300 *3.4. Benchmarking performance against a naïve model*

301 As a final performance evaluation, we benchmark our ML results against a simple model
302 of recurrence times constructed from an averaged recurrence interval for all events in a given
303 experiment (Figure 8). Because it assumes a statistical average of all recurrence intervals, this
304 model makes no implicit assumptions about and has no knowledge of the experiment or fault
305 behavior (Figure 8). With an $R^2 = 0.49$, the performance of this naïve model is relatively
306 unreliable. When compared with our ML models (Figures 5-7) which have R^2 metrics of 0.8 –
307 0.9 over the entire slip cycle, it is clear that the XGBoost models deliver superior performance.

308

309 **4. Discussion:**

310 *4.1. A physical basis for the evolution of fault zone elastic properties in the seismic cycle*

311 The evolution of elastic wave properties around fault zones has been extensively studied
312 in the laboratory (eg. *Stanchits et al., 2003; Paterson and Wong, 2005; Passelègue et al., 2018*)
313 and, to a smaller degree, on crustal faults (eg. *Niu et al., 2008; Brenguier et al., 2008; Malagnini*
314 *et al., 2019; Chiarabba et al., 2020*). Specifically, systematic variations in the p-wave velocity
315 field prior to fault failure in the laboratory over multiple slow and fast cycles has been
316 documented (*Kaproth and Marone, 2013; Tinti et al., 2016*) and attributed to preseismic creep
317 (*Scuderi et al., 2016*). Similarly, variations in p-wave amplitudes (or transmissivity or
318 transmission coefficient) have been documented as arising from preseismic creep (*Hedayat et al.,*
319 *2014; Shreedharan et al., 2020*). In crustal faults, *Malagnini et al. (2019)* observed a preseismic

320 attenuation signal in the 20-40 Hz frequency range leading up to the 2004 M6 Parkfield
 321 earthquake, which they attributed to fluctuations in the fault zone crack density. However, the
 322 ultrasonic amplitudes can be connected to the microscopic asperity stiffness and during stable
 323 sliding, the real area of contact (*Kendall and Tabor, 1971; Kilgore et al., 2017; Shreedharan et*
 324 *al., 2019*). Formalized mathematically, when the ultrasonic pulse wavelength is significantly
 325 larger than the fault zone width as is the case here, the specific interface stiffness, k_{sp} , is related
 326 to the transmissivity, $|T|$, as (*Pyrak-Nolte et al., 1990; Kilgore et al., 2017*)

$$327 \quad k_{sp} = \frac{\omega \rho v_p}{\sqrt{\frac{1}{|T|^2} - 1}} \quad (2)$$

328 Here, ρ is the density of the surrounding medium (Westerly granite) and v_p is the p-wave
 329 velocity through this medium. More recently, *Shreedharan et al. (2021)* demonstrated that while
 330 the ultrasonic amplitudes track fault creep, seismic velocity contains information about fault
 331 creep as well as shear stiffening of the wallrock. This ‘duality’ of information contained in the
 332 seismic velocities has been documented in crustal faults as well (*Chiarabba et al., 2020*).

333 Based on Eq. (2), the strong inverse correlation between wave amplitude and the fault
 334 zone slip rate (Figure 4) can be interpreted as the interseismic and coseismic evolution of fault
 335 zone asperity stiffness. More specifically, immediately following a stick-slip event, the fault
 336 locks up and heals interseismically (*Dieterich, 1972; Marone, 1998a; Kaproth and Marone,*
 337 *2014; McLaskey et al., 2012*). During this period, the increasing amplitudes and velocities can be
 338 interpreted as an increase in asperity stiffness due to reduced slip rate. Similarly, the reduction of
 339 precursory amplitude and velocity at and after the onset of preslip can be interpreted as a
 340 reduction in asperity stiffness (or, perhaps, asperity destruction) due to welded contact junctions
 341 being broken by fault slip. While not a prominent feature of this dataset (Figure 4), the
 342 amplitudes and velocities are nominally distinctly out of phase due to the additional information

343 pertaining to shear stiffening contained in the velocity (See Figure 2 of *Shreedharan et al.*,
 344 2021). In a physical model, this may be translated as an interseismic and preseismic reduction in
 345 wallrock crack density due to increased deviatoric stresses experienced by the wallrock during
 346 elastic strain energy build-up. Thus, by training our regression-based models on transmissivity
 347 and velocity, we are, by proxy, training our models on the systematic temporal evolution of the
 348 interface stiffness and bulk shear stiffening over multiple seismic cycles.

349

350 4.2. Connecting ML model response to the physics of frictional sliding

351 The supervised ML approach used in this study ‘learns’ from a regression between the
 352 features and labels; thus, no temporal information about a prior state of the fault is explicitly
 353 transferred from the experimental data to the ML model. At any point in time, the coefficient of
 354 friction, μ , of the fault can be expressed within the rate and state frictional framework as a
 355 function of the fault slip velocity, V , and a state evolution term, θ , as

$$356 \quad \mu = \mu_0 + a \ln\left(\frac{V}{V_0}\right) + b \ln\left(\frac{\theta}{\theta_0}\right) \quad (3)$$

357 Here, a and b are rate-state constants and the subscript ‘0’ denotes a reference variable.
 358 The frictional state term, at steady state is generally thought of as an average asperity lifetime
 359 and is described as the ratio of a characteristic slip distance, D_c , and the fault slip rate, V . The
 360 term θ can only be determined via an iterative inversion procedure by solving Eq. (3)
 361 simultaneously with a state-evolution law and an elastic coupling equation. However, Eq. (3) can
 362 be rearranged (*Nagata et al.*, 2012) to redefine frictional state as φ , where

$$363 \quad \varphi = b \ln\left(\frac{\theta}{\theta_0}\right) = \mu - \mu_0 - a \ln\left(\frac{V}{V_0}\right) \quad (4)$$

364 Phase plane cross-plots between the mechanical attributes of the fault (Figure 9a,b), i.e.,
 365 between the friction coefficient, slip rate and frictional state (estimated using Eq. 4 with $a =$

366 0.0091), show the inter-relationships between the rate and state parameters described in Eq. (3)
367 (*Marone, 1998b*). Similarly, cross-plots of the friction coefficient and the ultrasonic attributes
368 (Figure 9c,d) are the relationships studied by the XGBoost models to optimize regressions for
369 shear stress prediction (Figure 5). The phase plane plots in Figure 9 contain hysteretic loops for
370 ~10 slow and fast seismic cycles. Note the strong inverse correlation between the slip rate
371 (Figure 9a) and the ultrasonic attributes (Figure 9c-d). Likewise, the frictional state evolution
372 (Figure 9b) is more directly correlated with these attributes. Qualitatively, our data illustrate the
373 relationships between ultrasonic amplitudes and state suggested by *Nagata et al. (2014)*. This
374 implies a mechanical relationship between the physically determined asperity stiffness and the
375 more empirical frictional state, thought to be an average asperity or contact junction lifetime.
376 However, because our stick-slip cycles represent non-steady state, unstable slip behavior of the
377 fault, no quantitative relationships between these parameters can be derived (*Kame et al., 2014*;
378 *Shreedharan et al., 2019*).

379 Here, we consider the potential relationships between the ML model results (Figures 5-7)
380 and the physical basis for the variations in ultrasonic attributes throughout the seismic cycle
381 (Figure 9e). For a multi-contact interface composed of numerous contact junctions interseismic
382 healing phase is marked by increasing contact junction size and number of contacts. During this
383 period the ultrasonic amplitudes and velocities increase (*Ryan et al., 2018*). Subsequently, as the
384 fault creeps prior to failure, some of these contact junctions are destroyed and shrink in size or
385 cease to exist. This is marked by a reduction in the transmissivity and fault zone velocity
386 (*Shreedharan et al., 2021*). Finally, during the coseismic slip phase, a number of contact
387 junctions are broken and the fault slips, releasing the stored strain energy in these asperities.

388 Recall that, for shear stress prediction (Figure 5) and time-to-failure prediction (Figure 7),
389 the models perform somewhat poorly during the early portions of the seismic cycle, whereas the
390 model performance is remarkably accurate as the fault approaches failure. In the case of time-
391 since-failure prediction (Figure 6), this trend is reversed and the ML model predictions are
392 excellent post-seismically, immediately following a stick-slip event. This is consistent with the
393 observations of *Lubbers et al. (2018)* who documented that the cataloged AEs early in the
394 seismic cycle were better predictors of time-since-failure than time-to-failure. Surprisingly, our
395 observations are in contrast with the model of *Hulbert et al. (2019)*. They document an inverse
396 relationship between the duration of the next slip event and the acoustic energy early in the slip
397 cycle of the current event. We report data at the same normal stress and, in turn, the same
398 fractional asperity contact area (*Shreedharan et al., 2019*) for different stick-slip magnitudes
399 whereas *Hulbert et al. (2019)* observe this inverse relationship on data collected at different
400 normal stresses (and thus, different real contact areas). Because stick-slip magnitudes (*Leeman et*
401 *al., 2016*) and AE amplitudes (and energy) scale with normal stress (*Rivière et al., 2018*), the
402 different trends documented here and by *Hulbert et al. (2019)* could, in part, be explained by
403 normal stress dependence (or a lack thereof) in the experimental designs. Moreover, the
404 relationship between dynamics of AEs and active seismic data are unknown, which makes it
405 harder to compare the results directly. However, we note that *Hulbert et al. (2019)* document
406 better model fits to their shear stress data closer to failure rather than early in the seismic cycle.
407 Thus, our results are qualitatively consistent in this regard. Based on our observations of the
408 accurate model fits early in the cycle for time-since-failure and later in the cycle for time-to-
409 failure, we posit that the early, interseismic ultrasonic attributes have significant predictive
410 power and may contain information about the past state of the fault (Interseismic healing in

411 Figure 9e). This is qualitatively similar to the idea that aftershock duration may be linked to
412 mainshock size (*Dieterich, 1994; Lubbers et al., 2018*) although no evidence for this assertion
413 appears to exist in crustal faults (*Ziv, 2006*). Likewise, the ultrasonic attributes after the onset of
414 preslip likely contain predictive power about the future state of the fault (Preseismic creep phase
415 in Figure 9e), i.e., timing and size of the imminent failure (*Rouet-Leduc et al., 2017;*
416 *Shreedharan et al., 2020*).

417 For each of the ML feature sets we studied, the model performance suffers during the
418 middle of the seismic cycle, as the fault begins to unlock. We propose that this occurs because
419 the frictional asperities experience a competition between healing, which strengthens contact
420 junctions, and preslip, which rejuvenates contacts. These competing mechanisms translate into
421 nearly zero rate-of-change for the features (Figure 4) at the onset of preslip, which in turn, results
422 in poor regression fits because the monotonically varying data labels are associated with nearly
423 constant features. For instance, in the limited number of stick-slip instabilities plotted in Figure
424 9c,d, notice that the p-wave amplitudes and velocities are relatively constant at ~ 71 a.u. and 5719
425 m/s respectively, for friction coefficients in the range of 0.575 – 0.59, i.e., during the transition
426 from interseismic healing to preseismic creep.

427 Taken together, our ML model predictions (Figures 5-7) and the physical mechanisms
428 behind the evolution of the ultrasonic parameters (Figure 4, 9) indicate that even a relatively
429 simple regression, incorporating no explicit temporal information, can provide insights into the
430 mechanics of fault stability and earthquake nucleation, at least on the laboratory scale. More
431 specifically, because the ultrasonic (amplitude/velocity) evolution is physically related to healing
432 and preslip-driven interfacial asperity stiffness variations, and shear stiffening of the wallrock,

433 the ML model is able to infer the state of the fault and proximity to failure from these
434 microphysical variations.

435 These results have important implications for faulting and earthquake forecasting on the
436 crustal scale, particularly near shallow subduction zones (*Reasenberg, 1999*), and in regions
437 where elastodynamic foreshocks (*Dodge et al., 1996; Ellsworth and Bulut, 2018*) and slow
438 aseismic creep fronts (*Melbourne and Webb, 2002*) have been detected prior to a mainshock.
439 Preseismic crustal velocity anomalies have been observed prior to a limited number of
440 earthquakes (eg. *Niu et al., 2008; Chiarabba et al., 2020*). Thus, these ML methods could
441 potentially be applied to such regions and, particularly around repeating earthquakes or shallow
442 slow earthquakes, if velocity or attenuation trends are available over multiple seismic cycles.

443

444 **5. Conclusions:**

445 We study the feasibility of predicting the timing and shear stress of laboratory
446 earthquakes using high resolution measurements of transmitted wave amplitude and velocity.
447 Our data provide the first test of using active source seismic data to predict labquakes. We find
448 that supervised machine learning is capable of predicting the timing and shear stress state of
449 labquakes with reasonable accuracy. Moreover, our results indicate that post-seismic increases in
450 the ultrasonic amplitudes and velocities, often associated with fault and frictional healing, may
451 contain memory of the past state of the fault. Importantly, our predictions of fault time-to-failure
452 improve in accuracy prior to failure, indicating that fault preslip, which reduces ultrasonic
453 amplitude and velocity, has significant predictive power in the context of imminent failure.
454 Finally, the physical underpinning of the systematic changes in ultrasonic attributes is grounded
455 in the deformation mechanics and the evolution of stiffness of microscopic load-bearing

456 asperities. Hence, we are able to assign a physical model for the inner workings of predictive
457 ‘black-box’ ML models. Overall, our study demonstrates the utility of ML techniques in the
458 study of fault mechanics at the laboratory scale and serves to motivate future pursuits in the quest
459 to improve earthquake forecasting and hazard preparedness in crustal faults.

460

461

462 **Acknowledgements:**

463 We thank Steven Swavely for technical assistance. This study was supported by European
464 Research Council Advance Grant 835012 (TECTONIC), US Department of Energy grants DE-
465 SC0020512 and DE-EE0008763, and US National Science Foundation grants EAR 1520760,
466 EAR1547441, and EAR1763305 to CM. Data are available from PSU Scholarsphere
467 (<https://www.doi.org/10.26207/c4as-9s14>) or by contacting the corresponding author.

468

469 **Figures**

470 **Figure 1.** Data for one complete experiment showing the shear stress evolution as a function of
471 load point displacement. Unload-reload cycles at ~2 and 3 mm promote shear localization and
472 steady state shear. Training and test data come from 18-20 mm and 20-21 mm of shear
473 displacement, respectively. Insets show: schematic of the experiment setup, zoom of slow and
474 fast labquakes with definitions of time-since-failure (T_{prev}) and time-to-failure (T_{next}), and a
475 sample elastic wave with the wavelet (blue) used to measure p-wave travel time and amplitude.

476

477 **Figure 2.** Data labels (a,b) and feature engineering (c-f) for the ML models. (a) Shear stress over
478 multiple lab seismic cycles showing a complex range of stress drops and recurrence intervals; (b)
479 Time-since- (dashed) and time-to-failure (solid) for the events in Panel a; (c and d) raw (green)
480 and smoothed (black) p-wave amplitude (c) and velocity (d); (e and f) relative changes in p-wave
481 amplitude (e) and velocity (f) normalized against the start of each stick-slip cycle (black) and an
482 offset vector (blue) of the normalized amplitudes.

483

484 **Figure 3.** Complexity and periodicity of the labquake recurrence interval. (a) Cross-plot of time
485 elapsed since the previous event and time remaining to the next event colored by labquake stress
486 drop. Fiducial lines for 1:2 and 2:1 represent period doubling and 1:1 represents perfectly
487 periodic events. (b) Evolution of peak and minimum shear stress for multiple events in the
488 training and testing datasets, plotted by event number and thus increasing shear displacement.
489 Note that stress drop increases slightly with shear (c) Ratio of time since previous and time to
490 next event plotted by event number. The dashed lines at 0.5 and 2 represent the envelopes for
491 period doubling. A ratio of 1 represents perfectly periodic events.

492
493 **Figure 4.** Evolution of the mechanical and ultrasonic data over multiple laboratory seismic
494 cycles. Temporal evolution of (a) Shear stress (b) slip (black) and slip rate (blue) estimated from
495 the onboard slip sensor. Note that the fault is nearly locked for a big fraction of the seismic cycle
496 (c) Transmissivity and (d) p-wave velocity. Note that both transmitted wave amplitude (c) and
497 velocity show clear precursory changes prior to failure.

498
499 **Figure 5.** Shear stress prediction using ML. (a-c) Prediction using amplitudes as features
500 showing (a) Training (b) Testing dataset and (c) model performance expressed as a cross-plot of
501 experimental shear stress versus ML model results with 1:1 line indicating perfect model
502 accuracy. (d-f) Prediction using velocities as features showing (d) Training (e) testing dataset and
503 (c) model performance. Detailed comparison for a representative seismic cycle showing data
504 (black) and model (blue) trained on amplitude (g) and velocity(h). In both panels the lower plot
505 (grey) shows the RMSE misfit.

506

507 **Figure 6.** Time-since-failure prediction. (a-c) Prediction using amplitudes as features showing
508 (a) Training (b) Testing dataset and (c) model performance expressed as a cross-plot of
509 experimental shear stress versus ML model results with 1:1 line indicating perfect model
510 accuracy. (d-f) Prediction using velocities as features showing (d) Training (e) testing dataset and
511 (c) model performance. Detailed comparison for a representative seismic cycle showing data
512 (black) and model (blue) trained on amplitude (g) and velocity(h). In both panels the lower plot
513 (grey) shows the RMSE misfit.

514

515 **Figure 7.** Time-to-failure prediction. (a-c) Prediction using amplitudes as features showing (a)
516 Training (b) Testing dataset and (c) model performance expressed as a cross-plot of experimental
517 shear stress versus ML model results with 1:1 line indicating perfect model accuracy. (d-f)
518 Prediction using velocities as features showing (d) Training (e) testing dataset and (c) model
519 performance Detailed comparison for a representative seismic cycle showing data (black) and
520 model (blue) trained on amplitude (g) and velocity(h). In both panels the lower plot (grey)
521 shows the RMSE misfit.

522

523 **Figure 8.** Naïve model for benchmarking performance. Time to failure for the experimental data
524 (black) and a model (green) based on constant recurrence interval. The low R^2 value shows that
525 the naïve model predicts earthquake failure times poorly.

526

527 **Figure 9.** Phase plane cross-plots of (a) friction and slip velocity expressed as a ratio of the slip
528 velocity to loading rate on a logarithmic scale (b) friction and frictional state expressed on a
529 logarithmic scale (c) friction and p-wave amplitudes (d) p-wave velocity. The interseismic

530 locking (green), preseismic creep (blue) and coseismic slip (orange) phases are annotated in each
 531 plot.

532

533 **References**

534 Bakun, W. H., Aagaard, B., Dost, B., Ellsworth, W. L., Hardebeck, J. L., Harris, R. A., ... &
 535 Michael, A. J. (2005). Implications for prediction and hazard assessment from the 2004
 536 Parkfield earthquake. *Nature*, 437(7061), 969-974.

537 Bergen, K. J., Johnson, P. A., Maarten, V., & Beroza, G. C. (2019). Machine learning for data-
 538 driven discovery in solid Earth geoscience. *Science*, 363(6433).

539 Bolton, D. C., Shokouhi, P., Rouet-Leduc, B., Hulbert, C., Rivière, J., Marone, C., & Johnson, P.
 540 A. (2019). Characterizing acoustic signals and searching for precursors during the laboratory
 541 seismic cycle using unsupervised machine learning. *Seismological Research Letters*, 90(3),
 542 1088-1098.

543 Bolton, D. C., Shreedharan, S., Rivière, J., & Marone, C. (2020). Acoustic Energy Release
 544 During the Laboratory Seismic Cycle: Insights on Laboratory Earthquake Precursors and
 545 Prediction. *Journal of Geophysical Research: Solid Earth*, 125(8), e2019JB018975.

546 Brace, W. F., Paulding Jr, B. W., & Scholz, C. H. (1966). Dilatancy in the fracture of crystalline
 547 rocks. *Journal of Geophysical Research*, 71(16), 3939-3953.

548 Brenguier, F., Campillo, M., Hadziioannou, C., Shapiro, N. M., Nadeau, R. M., & Larose, E.
 549 (2008). Postseismic relaxation along the San Andreas fault at Parkfield from continuous
 550 seismological observations. *science*, 321(5895), 1478-1481.

551 Chen, T., & Guestrin, C. (2016, August). Xgboost: A scalable tree boosting system.
 552 In *Proceedings of the 22nd acm sigkdd international conference on knowledge discovery and*
 553 *data mining* (pp. 785-794).

554 Chiarabba, C., De Gori, P., Segou, M., & Cattaneo, M. (2020). Seismic velocity precursors to the
 555 2016 Mw 6.5 Norcia (Italy) earthquake. *Geology*.

556 Corbi, F., Sandri, L., Bedford, J., Funicello, F., Brizzi, S., Rosenau, M., & Lallemand, S. (2019).
 557 Machine learning can predict the timing and size of analog earthquakes. *Geophysical*
 558 *Research Letters*, 46. [https://doi.org/ 10.1029/2018GL081251](https://doi.org/10.1029/2018GL081251)

559 Corbi, F., Bedford, J., Sandri, L., Funicello, F., Gualandi, A., & Rosenau, M. (2020). Predicting
 560 imminence of analog megathrust earthquakes with Machine Learning: Implications for
 561 monitoring subduction zones. *Geophysical Research Letters*, 47(7), e2019GL086615.

562 Dieterich, J. H. (1972). Time-dependent friction in rocks. *Journal of Geophysical*
 563 *Research*, 77(20), 3690-3697.

564 Dieterich, J. (1994). A constitutive law for rate of earthquake production and its application to
 565 earthquake clustering. *Journal of Geophysical Research: Solid Earth*, 99(B2), 2601-2618.

566 Dodge, D. A., Beroza, G. C., & Ellsworth, W. L. (1996). Detailed observations of California
 567 foreshock sequences: Implications for the earthquake initiation process. *Journal of*
 568 *Geophysical Research: Solid Earth*, 101(B10), 22371-22392.

569 Ellsworth, W. L., & Bulut, F. (2018). Nucleation of the 1999 Izmit earthquake by a triggered
 570 cascade of foreshocks. *Nature Geoscience*, 11(7), 531-535.

- 571 Friedman, J. H. (2001). Greedy function approximation: a gradient boosting machine. *Annals of*
572 *statistics*, 1189-1232.
- 573 Gu, J. C., Rice, J. R., Ruina, A. L., & Simon, T. T. (1984). Slip motion and stability of a single
574 degree of freedom elastic system with rate and state dependent friction. *Journal of the*
575 *Mechanics and Physics of Solids*, 32(3), 167-196.
- 576 Hedayat, A., Pyrak-Nolte, L. J., & Bobet, A. (2014). Precursors to the shear failure of rock
577 discontinuities. *Geophysical Research Letters*, 41(15), 5467-5475.
- 578 Hulbert, C., Rouet-Leduc, B., Johnson, P. A., Ren, C. X., Rivière, J., Bolton, D. C., & Marone,
579 C. (2019). Similarity of fast and slow earthquakes illuminated by machine learning. *Nature*
580 *Geoscience*, 12(1), 69-74.
- 581 Hulbert, C., Rouet-Leduc, B., Jolivet, R., & Johnson, P. A. (2020). An exponential build-up in
582 seismic energy suggests a months-long nucleation of slow slip in Cascadia. *Nature*
583 *communications*, 11(1), 1-8.
- 584 Jones, D. R., Schonlau, M., & Welch, W. J. (1998). Efficient global optimization of expensive
585 black-box functions. *Journal of Global optimization*, 13(4), 455-492.
- 586 Kame, N., Nagata, K., Nakatani, M., & Kusakabe, T. (2014). Feasibility of acoustic monitoring
587 of strength drop precursory to earthquake occurrence. *Earth, Planets and Space*, 66(1), 41.
- 588 Kaproth, B. M., & Marone, C. (2013). Slow earthquakes, preseismic velocity changes, and the
589 origin of slow frictional stick-slip. *Science*, 341(6151), 1229-1232.
- 590 Kaproth, B. M., and C. Marone, Evolution of elastic wave speed during shear-induced damage
591 and healing within laboratory fault zones, *J. Geophys. Res. Solid Earth*, 119,
592 10.1002/2014JB011051, 2014.
- 593 Karner, S. L., & Marone, C. (1998). The effect of shear load on frictional healing in simulated
594 fault gouge. *Geophysical research letters*, 25(24), 4561-4564.
- 595 Kendall, K., & Tabor, D. (1971). An ultrasonic study of the area of contact between stationary
596 and sliding surfaces. *Proceedings of the Royal Society of London. A. Mathematical and*
597 *Physical Sciences*, 323(1554), 321-340.
- 598 Kilgore, B., Beeler, N. M., Lozos, J., & Oglesby, D. (2017). Rock friction under variable normal
599 stress. *Journal of Geophysical Research: Solid Earth*, 122(9), 7042-7075.
- 600 Kong, Q., Trugman, D. T., Ross, Z. E., Bianco, M. J., Meade, B. J., & Gerstoft, P. (2019).
601 Machine learning in seismology: Turning data into insights. *Seismological Research Letters*,
602 90(1), 3-14.
- 603 Leeman, J. R., Saffer, D. M., Scuderi, M. M., & Marone, C. (2016). Laboratory observations of
604 slow earthquakes and the spectrum of tectonic fault slip modes. *Nature communications*, 7(1),
605 1-6.
- 606 Lubbers, N., Bolton, D. C., Mohd-Yusof, J., Marone, C., Barros, K., & Johnson, P. A. (2018).
607 Earthquake catalog-based machine learning identification of laboratory fault states and the
608 effects of magnitude of completeness. *Geophysical Research Letters*, 45(24), 13-269.
- 609 Main, I. G., Bell, A. F., Meredith, P. G., Geiger, S., & Touati, S. (2012). The dilatancy–diffusion
610 hypothesis and earthquake predictability. *Geological Society, London, Special*
611 *Publications*, 367(1), 215-230.
- 612 Malagnini, L., Dreger, D. S., Bürgmann, R., Munafò, I., & Sebastiani, G. (2019). Modulation of
613 seismic attenuation at Parkfield, before and after the 2004 M6 earthquake. *Journal of*
614 *Geophysical Research: Solid Earth*, 124(6), 5836-5853.
- 615 Marone, C. (1998a). The effect of loading rate on static friction and the rate of fault healing
616 during the earthquake cycle. *Nature*, 391(6662), 69-72.

- 617 Marone, C. (1998b). Laboratory-derived friction laws and their application to seismic
618 faulting. *Annual Review of Earth and Planetary Sciences*, 26(1), 643-696.
- 619 McBeck, J., Aiken, J. M., Ben-Zion, Y., & Renard, F. (2020). Predicting the proximity to
620 macroscopic failure using local strain populations from dynamic in situ X-ray tomography
621 triaxial compression experiments on rocks. *Earth and Planetary Science Letters*, 543, 116344.
- 622 McBrearty, I. W., Delorey, A. A., & Johnson, P. A. (2019). Pairwise association of seismic
623 arrivals with convolutional neural networks. *Seismological Research Letters*, 90(2A), 503-
624 509.
- 625 McLaskey, G. C., Thomas, A. M., Glaser, S. D., & Nadeau, R. M. (2012). Fault healing
626 promotes high-frequency earthquakes in laboratory experiments and on natural
627 faults. *Nature*, 491(7422), 101-104.
- 628 Melbourne, T. I., & Webb, F. H. (2002). Precursory transient slip during the 2001 Mw= 8.4 Peru
629 earthquake sequence from continuous GPS. *Geophysical Research Letters*, 29(21), 28-1.
- 630 Mousavi, S. M., Ellsworth, W. L., Zhu, W., Chuang, L. Y., & Beroza, G. C. (2020). Earthquake
631 transformer—an attentive deep-learning model for simultaneous earthquake detection and
632 phase picking. *Nature communications*, 11(1), 1-12.
- 633 Nagata, K., Nakatani, M., & Yoshida, S. (2012). A revised rate-and state-dependent friction law
634 obtained by constraining constitutive and evolution laws separately with laboratory data.
635 *Journal of Geophysical Research: Solid Earth*, 117(B2).
- 636 Nagata, K., Kilgore, B., Beeler, N., & Nakatani, M. (2014). High-frequency imaging of elastic
637 contrast and contact area with implications for naturally observed changes in fault
638 properties. *Journal of Geophysical Research: Solid Earth*, 119(7), 5855-5875.
- 639 Niu, F., Silver, P. G., Daley, T. M., Cheng, X., & Majer, E. L. (2008). Preseismic velocity
640 changes observed from active source monitoring at the Parkfield SAFOD drill
641 site. *Nature*, 454(7201), 204-208.
- 642 Olivier, Gerrit, Julien Chaput, and Brian Borchers. "Using supervised machine learning to
643 improve active source signal retrieval." *Seismological Research Letters* 89.3 (2018): 1023-
644 1029.
- 645 Passelègue, F. X., Pimienta, L., Faulkner, D., Schubnel, A., Fortin, J., & Guéguen, Y. (2018).
646 Development and Recovery of Stress-Induced Elastic Anisotropy During Cyclic Loading
647 Experiment on Westerly Granite. *Geophysical Research Letters*, 45(16), 8156-8166.
- 648 Perol, T., Gharbi, M., & Denolle, M. (2018). Convolutional neural network for earthquake
649 detection and location. *Science Advances*, 4(2), e1700578.
- 650 Pyrak-Nolte, L. J., Myer, L. R., & Cook, N. G. (1990). Transmission of seismic waves across
651 single natural fractures. *Journal of Geophysical Research: Solid Earth*, 95(B6), 8617-8638.
- 652 Reasenber, P. A. (1999). Foreshock occurrence before large earthquakes. *Journal of*
653 *Geophysical Research: Solid Earth*, 104(B3), 4755-4768.
- 654 Ren, C. X., Peltier, A., Ferrazzini, V., Rouet-Leduc, B., Johnson, P. A., & Brenguier, F. (2020).
655 Machine learning reveals the seismic signature of eruptive behavior at piton de la fournaise
656 volcano. *Geophysical Research Letters*, 47(3), e2019GL085523.
- 657 Rivière, J., Lv, Z., Johnson, P. A., & Marone, C. (2018). Evolution of b-value during the seismic
658 cycle: Insights from laboratory experiments on simulated faults. *Earth and Planetary Science*
659 *Letters*, 482, 407-413.
- 660 Ross, Z. E., Meier, M. A., Hauksson, E., & Heaton, T. H. (2018). Generalized seismic phase
661 detection with deep learning. *Bulletin of the Seismological Society of America*, 108(5A),
662 2894-2901.

- 663 Rouet-Leduc, B., Hulbert, C., Lubbers, N., Barros, K., Humphreys, C. J., & Johnson, P. A.
 664 (2017). Machine learning predicts laboratory earthquakes. *Geophysical Research*
 665 *Letters*, 44(18), 9276-9282.
- 666 Rouet-Leduc, B., Hulbert, C., Bolton, D. C., Ren, C. X., Riviere, J., Marone, C., ... & Johnson, P.
 667 A. (2018). Estimating fault friction from seismic signals in the laboratory. *Geophysical*
 668 *Research Letters*, 45(3), 1321-1329.
- 669 Rouet-Leduc, B., Hulbert, C., & Johnson, P. A. (2019). Continuous chatter of the Cascadia
 670 subduction zone revealed by machine learning. *Nature Geoscience*, 12(1), 75-79.
- 671 Ryan, K. L., Rivière, J., & Marone, C. (2018). The role of shear stress in fault healing and
 672 frictional aging. *Journal of Geophysical Research: Solid Earth*, 123(12), 10-479.
- 673 Sammonds, P. R., Meredith, P. G., & Main, I. G. (1992). Role of pore fluids in the generation of
 674 seismic precursors to shear fracture. *Nature*, 359(6392), 228-230.
- 675 Scuderi, M. M., Marone, C., Tinti, E., Di Stefano, G., & Collettini, C. (2016). Precursory
 676 changes in seismic velocity for the spectrum of earthquake failure modes. *Nature*
 677 *geoscience*, 9(9), 695-700.
- 678 Scholz, C. H. (1968). Microfracturing and the inelastic deformation of rock in compression.
 679 *Journal of Geophysical Research*, 73(4), 1417-1432.
- 680 Shimazaki, K., & Nakata, T. (1980). Time-predictable recurrence model for large earthquakes.
 681 *Geophysical Research Letters*, 7(4), 279-282.
- 682 Shreedharan, S., Rivière, J., Bhattacharya, P., & Marone, C. (2019). Frictional state evolution
 683 during normal stress perturbations probed with ultrasonic waves. *Journal of Geophysical*
 684 *Research: Solid Earth*, 124(6), 5469-5491.
- 685 Shreedharan, S., Bolton, D. C., Rivière, J., & Marone, C. (2020). Preseismic fault creep and
 686 elastic wave amplitude precursors scale with lab earthquake magnitude for the continuum of
 687 tectonic failure modes. *Geophysical Research Letters*, 47(8), e2020GL086986.
- 688 Shreedharan, S., Bolton, D. C., Rivière, J., & Marone, C. (2021). Competition between preslip
 689 and deviatoric stress modulates precursors for laboratory earthquakes. *Earth and Planetary*
 690 *Science Letters*.
- 691 Stanchits, S. A., Lockner, D. A., & Ponomarev, A. V. (2003). Anisotropic changes in P-wave
 692 velocity and attenuation during deformation and fluid infiltration of granite. *Bulletin of the*
 693 *Seismological Society of America*, 93(4), 1803-1822.
- 694 Tan, P. N., M. Steinbach, and V. Kumar (2006). Cluster analysis: basic concepts and algorithms,
 695 in *Introduction to Data Mining*, Vol. 8, Addison-Wesley, Boston, Massachusetts, 487-568.
- 696 Tinti, E., Scuderi, M., Scognamiglio, L., Di Stefano, G., Marone, C., & Collettini, C. (2016). On
 697 the evolution of elastic properties during laboratory stick-slip experiments spanning the
 698 transition from slow slip to dynamic rupture. *Journal of Geophysical Research: Solid Earth*,
 699 121(12), 8569-8594.
- 700 Trugman, D. T., & Ross, Z. E. (2019). Pervasive foreshock activity across southern California.
 701 *Geophysical Research Letters*, 46(15), 8772-8781.
- 702 Veedu, D.M., Giorgetti, C., Scuderi, M., Barbot, S., Marone, C., & Collettini, C. (2020).
 703 Bifurcations at the Stability Transition of Earthquake Faulting. *Geophysical Research*
 704 *Letters*, 47(19), e2020GL087985.
- 705 Wu, Y., Lin, Y., Zhou, Z., Bolton, D. C., Liu, J., & Johnson, P. (2018). DeepDetect: A cascaded
 706 region-based densely connected network for seismic event detection. *IEEE Transactions on*
 707 *Geoscience and Remote Sensing*, 57(1), 62-75.

- 708 Yoon, C. E., O'Reilly, O., Bergen, K. J., & Beroza, G. C. (2015). Earthquake detection through
709 computationally efficient similarity search. *Science advances*, 1(11), e1501057.
- 710 Zhu, W., & Beroza, G. C. (2019). PhaseNet: a deep-neural-network-based seismic arrival-time
711 picking method. *Geophysical Journal International*, 216(1), 261-273.
- 712 Ziv, A. (2006). Does aftershock duration scale with mainshock size?. *Geophysical research*
713 *letters*, 33(17).

Figure 1.

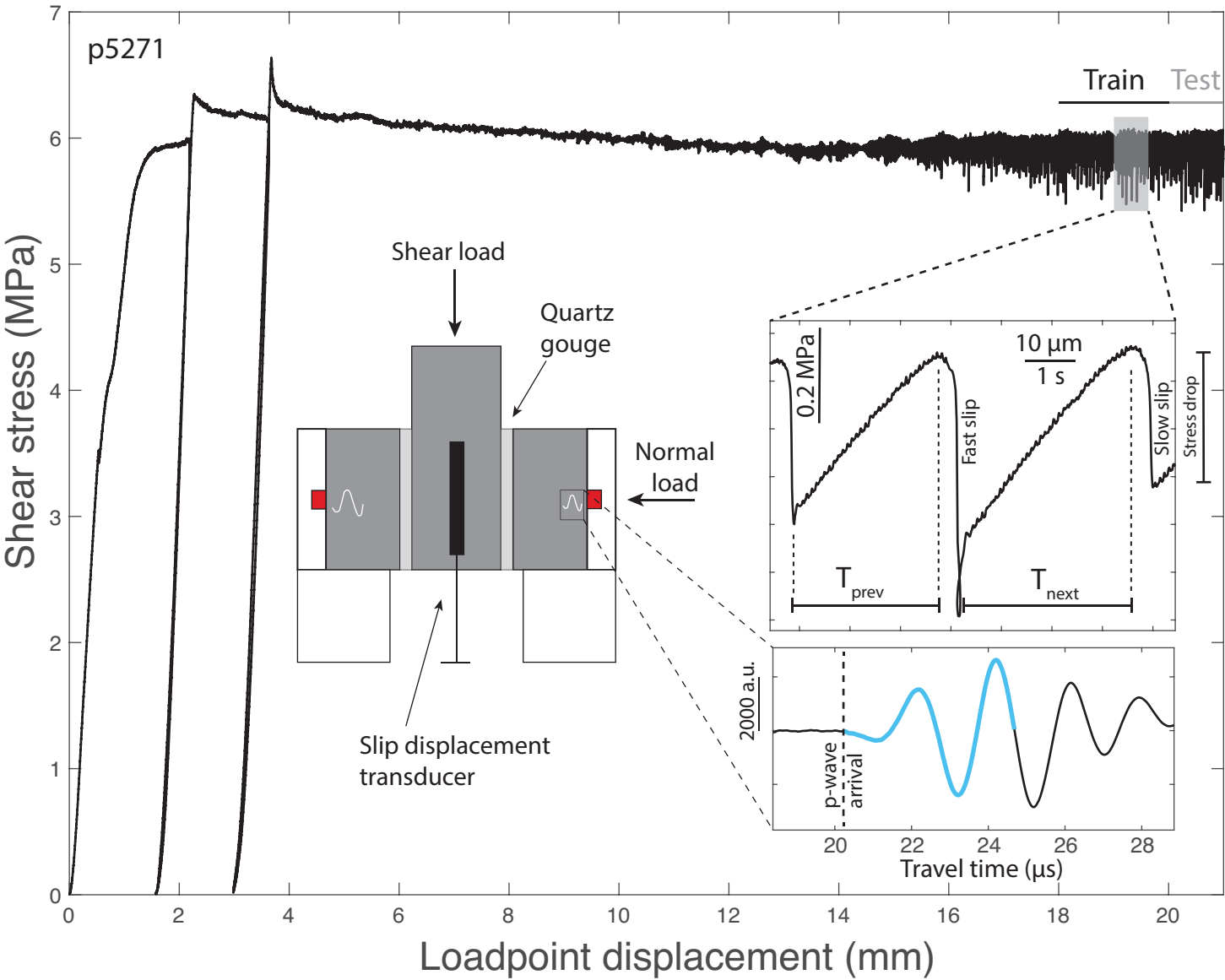


Figure 2.

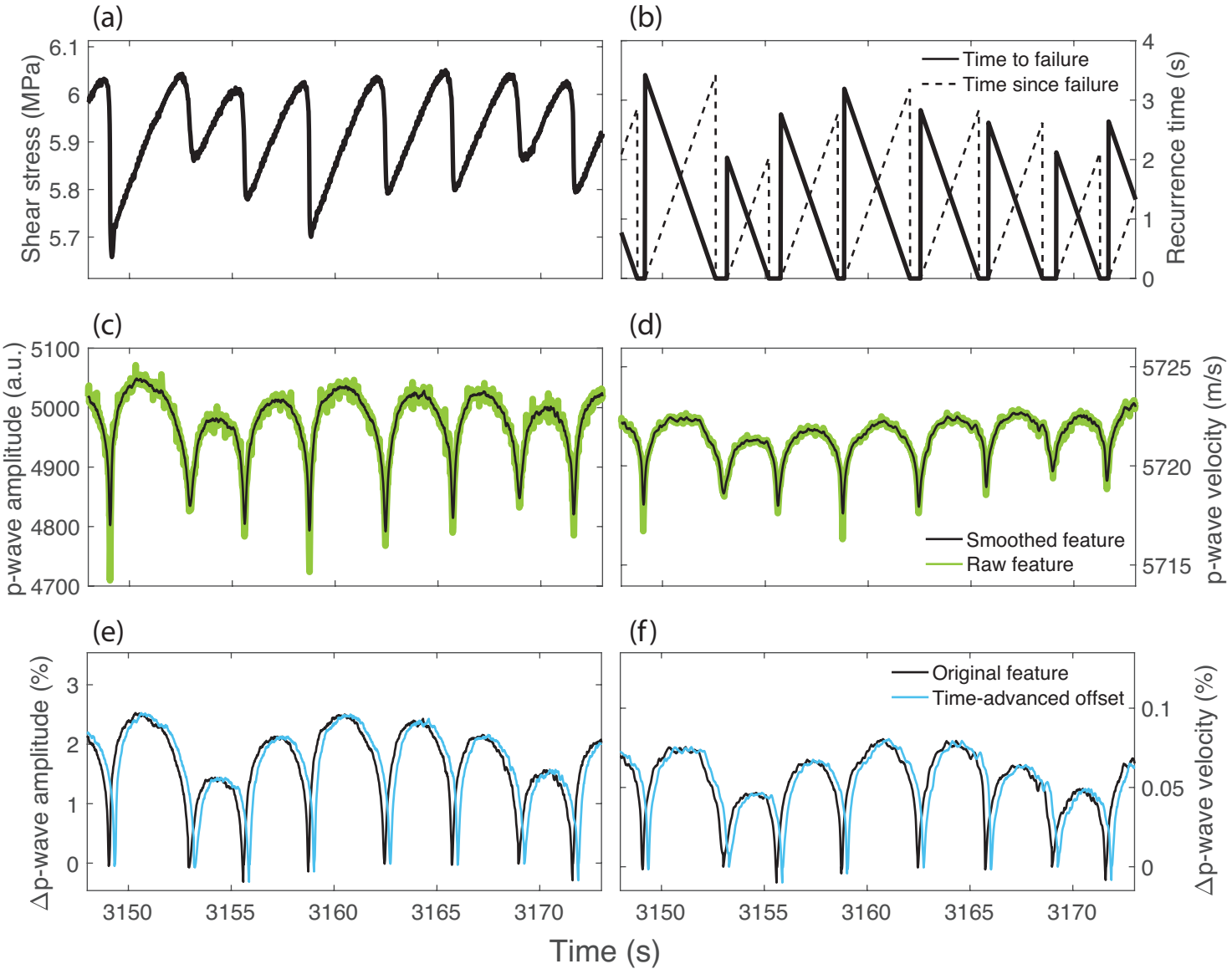


Figure 3.

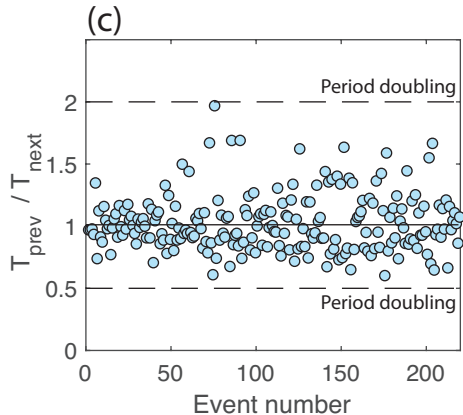
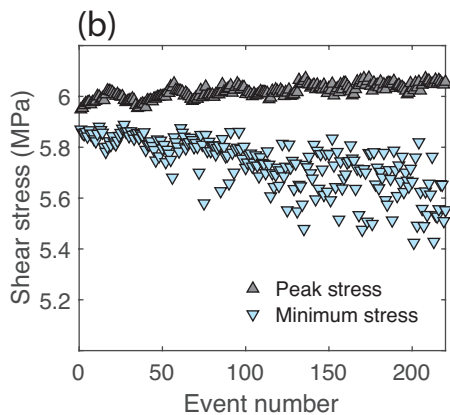
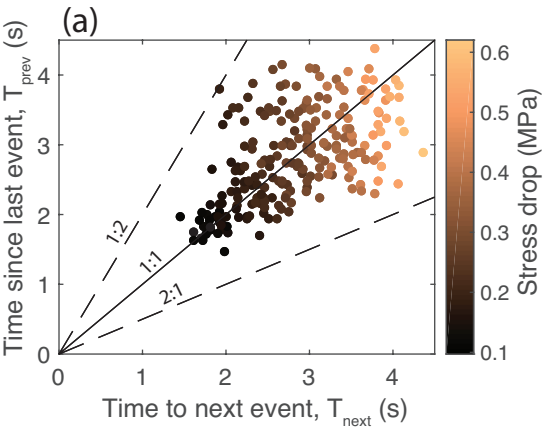


Figure 4.

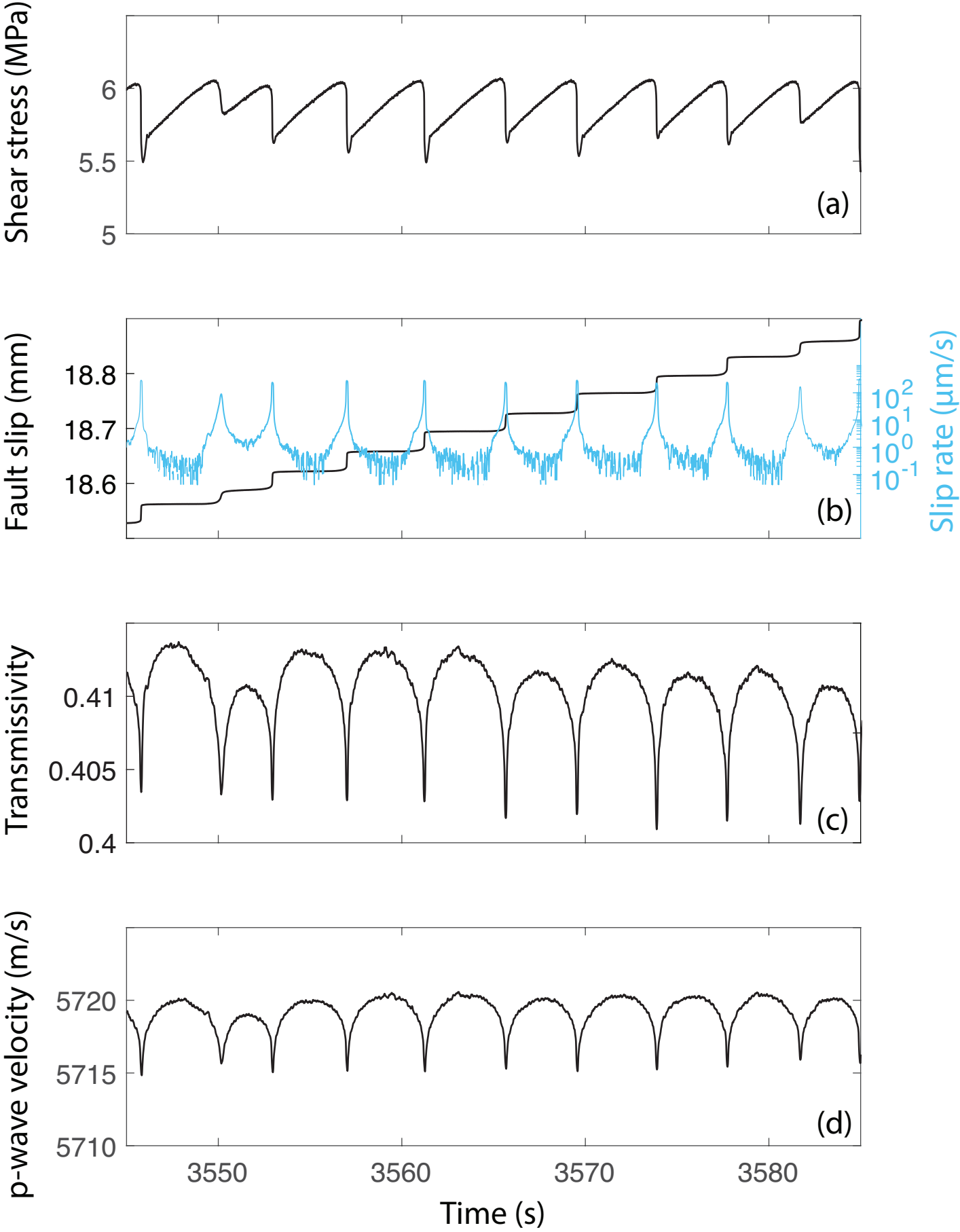


Figure 5.

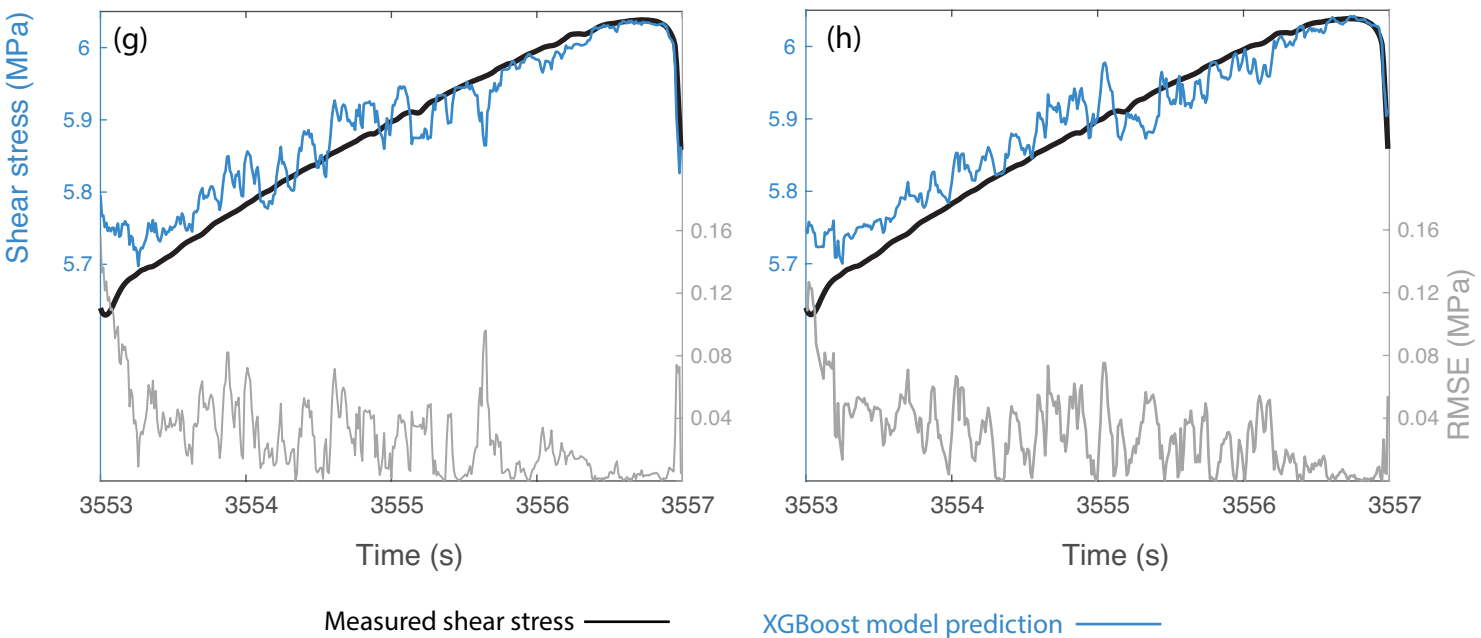
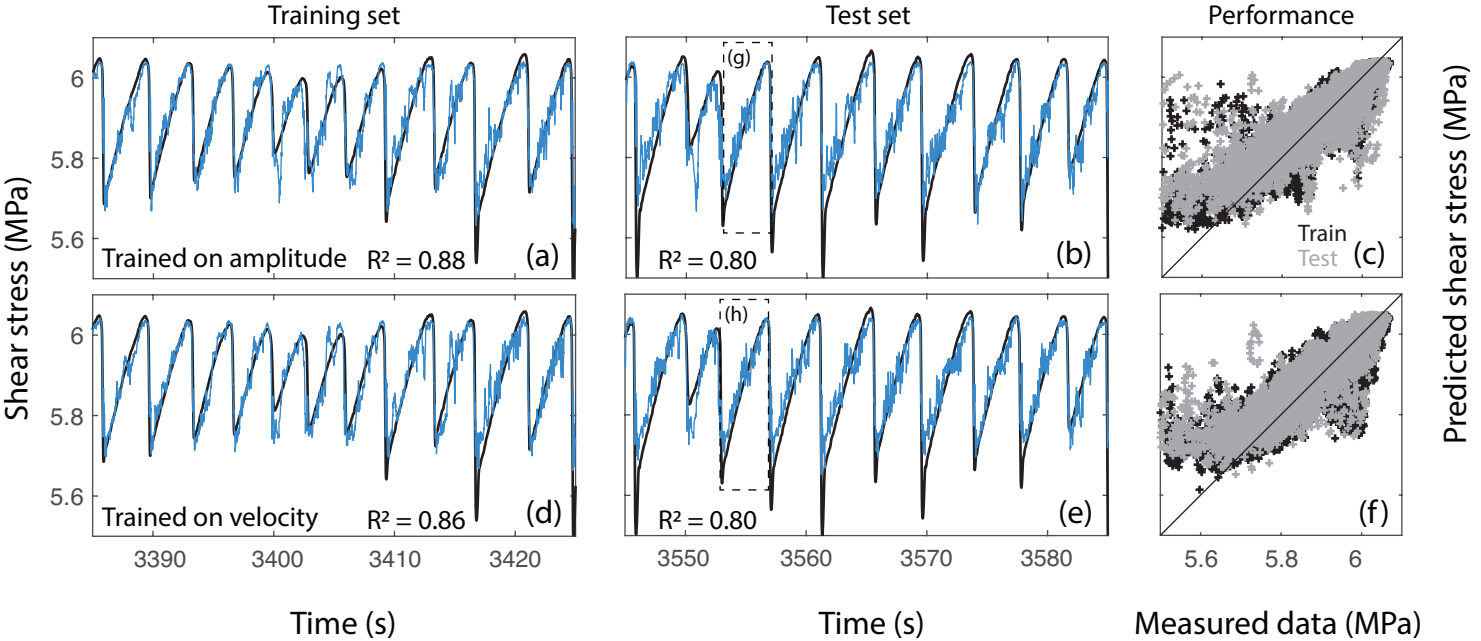


Figure 6.

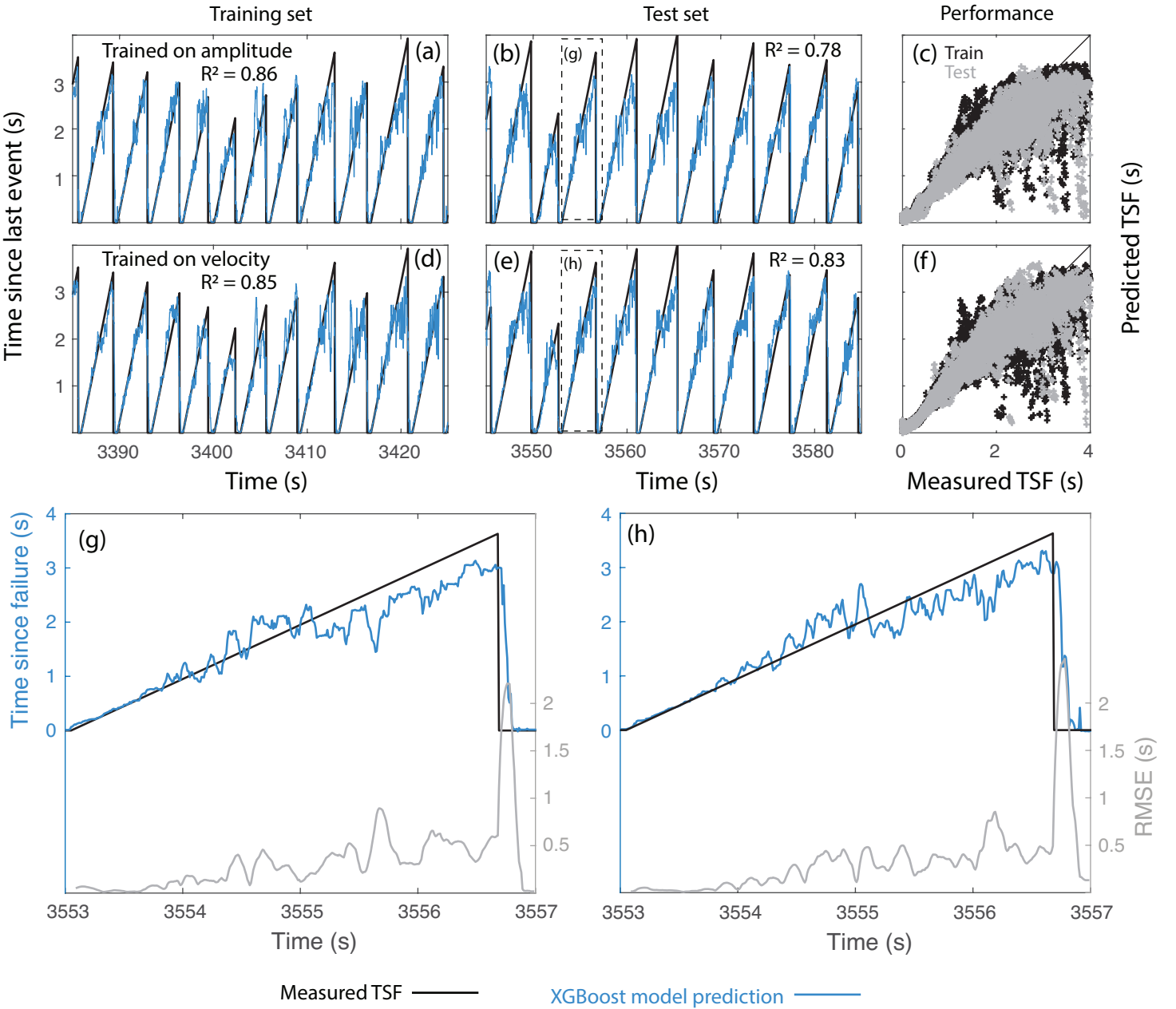


Figure 7.

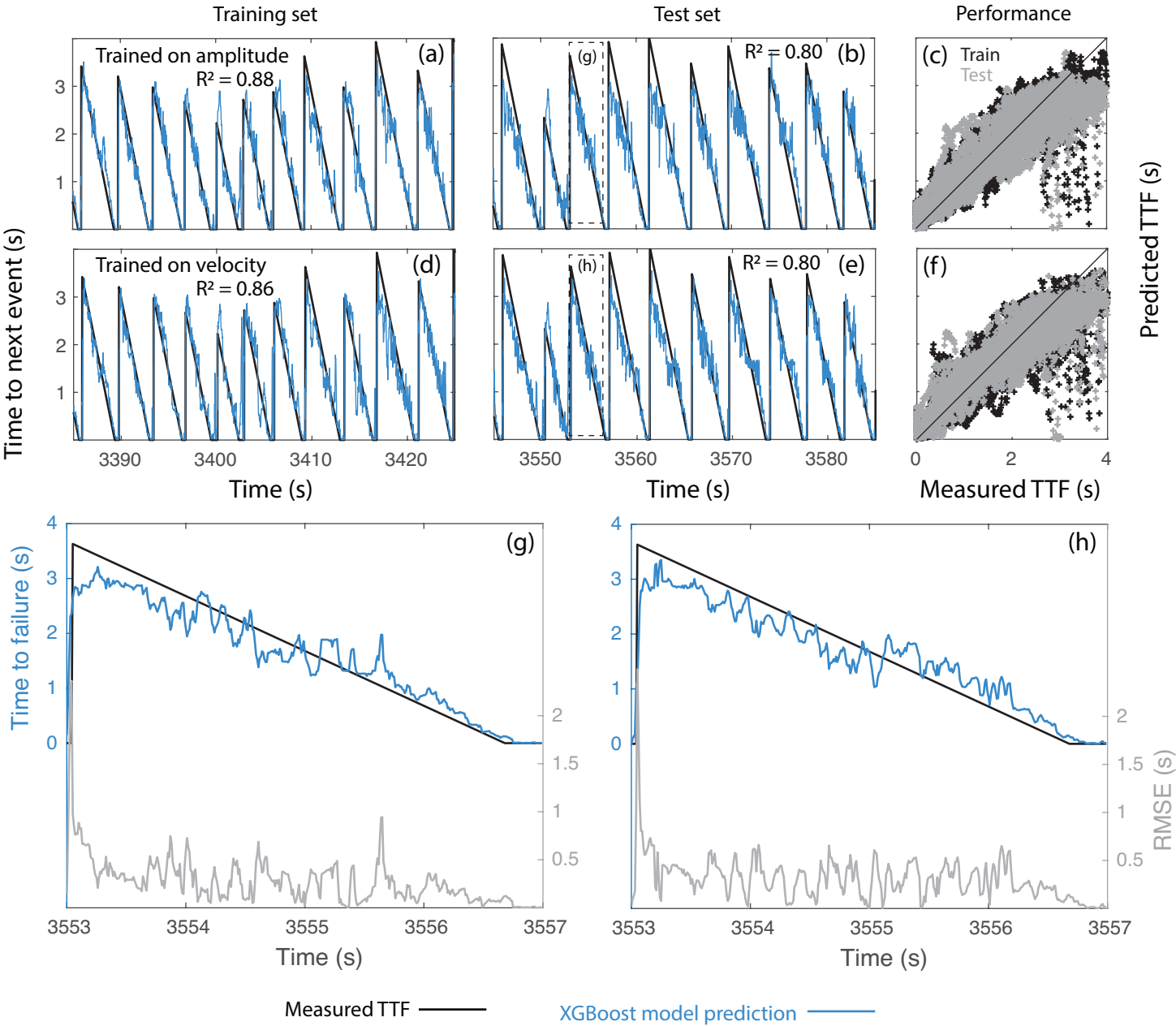


Figure 8.

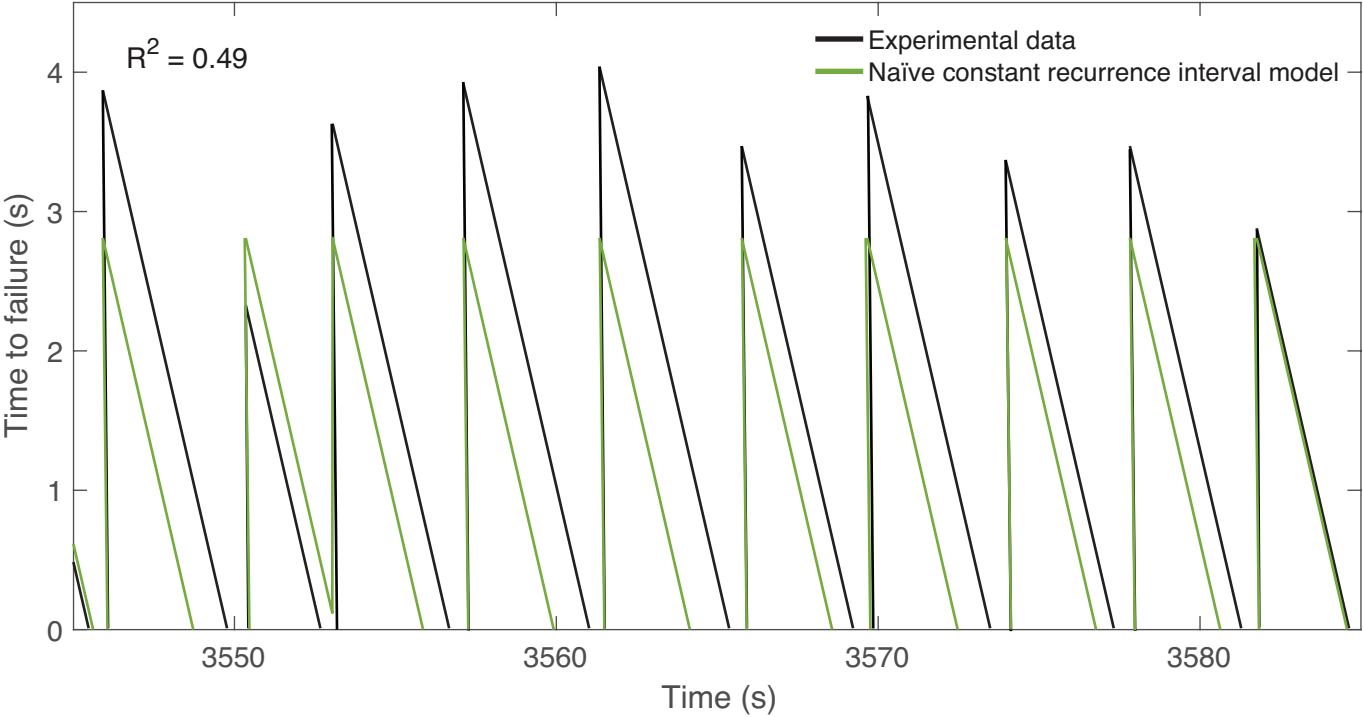


Figure 9.

